Nano Research

Open Access

Research Article

Boosting syngas production in photoelectrochemical CO_2 reduction through organic molecule interaction with copper photoanodes

Chenchen Zhang[1], Chaofeng Chen[1], Junjun Mao[1], Dan Wang[1], Peng Luan[2], Qingqing Song[1], Yuanming Xie[1], Yao Wang[1]✉, Yong Zhao[3]✉, Ying Zhang[1]✉, and Yongfa Zhu[4]

[1] *Key Laboratory of Synthetic and Biological Colloids Ministry of Education, School of Chemical and Material Engineering, Jiangnan University, Wuxi 214122, China*
[2] *State Key Laboratory of Catalysis, Dalian National Laboratory for Clean Energy, Dalian Institute of Chemical Physics, Chinese Academy of Sciences, Dalian 116023, China*
[3] *CSIRO Energy Centre, Mayfield West, NSW 2304, Australia*
[4] *Department of Chemistry, Tsinghua University, Beijing 100084, China*

Cite this article: *Nano Research*, **2025**, *18*, 94907306. https://doi.org/10.26599/NR.2025.94907306

ABSTRACT: Photoelectrochemical syngas production using photoanode-driven systems from aqueous CO_2 is a promising technology. To address the challenge of poor selectivity caused by the wide band gap of photoelectrode, we introduce a novel photoanode, PDI/Cu_2O/Cu, where PDI is the perylene tetracarboxylic di-(propyl imidazole). Using Cu_2O as a substrate enhances charge transfer kinetics, while PDI modification mitigates photocorrosion and augments photoelectrochemical CO_2 reduction reaction (PEC CO_2RR) activity. This enhancement stems from PDI's narrow band gap and efficient visible light absorption. The syngas production achieved a noteworthy 124.47 μmol/(cm²·h) at 1.57 V vs. RHE, making it an optimal feedstock gas for hydrocarbon synthesis. Detailed UV–vis spectra indicate that layered structure significantly improves the absorption edge of the photoanode, facilitating enhanced utilization of visible light. Additionally, the electron lifetime of the PDI/Cu_2O/Cu photoanode is substantially increased which is also one of the factors affecting the reactivity, as demonstrated by the Bode phase plot.

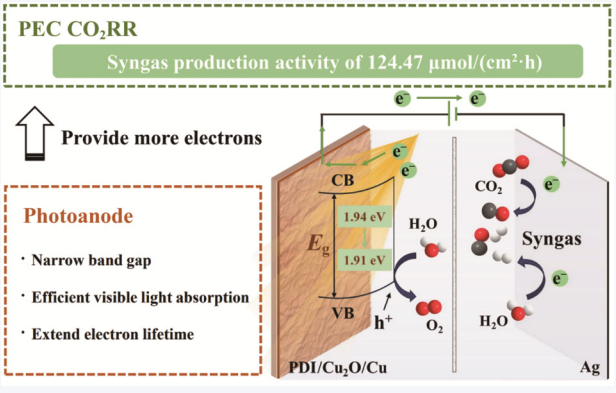

KEYWORDS: photoelectrochemical (PEC) CO_2 reduction, syngas production, photoanode, metal-organic framework (MOF)

1 Introduction

Photoelectrochemical (PEC) CO_2 reduction reaction (CO_2RR), which utilizes sunlight to drive the direct conversion of CO_2 into syngas, is widely regarded as an effective strategy to diminish carbon emissions and store intermittent solar energy [1, 2]. Compared with electrochemical CO_2RR [3, 4], the photovoltage is able to supplement the battery voltage to reduce the overpotential of the overall reaction [5, 6]. Currently, most of the researches widely focused on the performance of the working electrode during the PEC CO_2RR, while the anode can signifcantly infuence the cathode and plays an important role.

Photoanode materials [7–10], with high Fermi energy level, facilitate upward band bending and hole accumulation in the solution. It is capable of releasing electrons into external circuits through the absorption of light energy, providing a sizable potential energy output. Therefore, it has a competitive advantage in absorbing photons and generating electrons during PEC water oxidation, which contributes to the realization of cathodic CO_2 reduction. For instance, materials such as TiO_2, Si, $BiVO_4$, and WO_3 act as photoanodes to reduce the voltage required for the CO_2RR and exhibit commendable performance. However, it should be noted that the optical absorption range of most photoanodes is relatively narrow. For example, the typical ultraviolet (UV)-sensitive

Received: January 15, 2025; **Revised:** February 10, 2025
Accepted: February 13, 2025

✉Address correspondence to Ying Zhang, ying.zhang@jiangnan.edu.cn; Yong Zhao, y.zhao@csiro.au; Yao Wang, wangyao@jiangnan.edu.cn

TiO_2 photoanodes absorb visible light weakly [11]. Besides, tranditional photoanodes with wide band gap perform less well in the separation of photogenerated electrons and photogenerated holes, resulting in low charge utilization [12]. Therefore, the performance of photoanodes remains limited to some extent. Consequently, the integration of photoanodes into the process of PEC CO_2RR continues to represent a significant, outstanding challenge.

Cu_2O, synthesized with a high carrier concentration, serves as a promising substrate for the photoanode working electrode, enhancing interfacial charge transfer kinetics effectively [13, 14]. However, Cu_2O semiconductor catalysts are commonly susceptible to photocorrosion, resulting in reduced activity and limited stability [15]. To weaken the photocorrosion of Cu_2O, further reduce the photoanodic band gap and widen the optical absorption range of photoanode, the introduction of perylene tetracarboxylic di-(propyl imidazole) (PDI) plays an important role. PDI, as an organic supramolecular photocatalyst, offers several advantages, including a straightforward synthesis method, effective absorption of visible light, and outstanding photocatalytic activity [16]. PDI has a narrow band gap (< 2 eV) and a high band edge oxidation potential [17, 18]. Hence, PDI finds extensive application in the realm of photocatalysis.

In this study, we electrochemically deposited Cu_2O thin films onto a copper substrate, ensuring favorable electron transfer kinetics, and further modified the surface with a layer of PDI through a solid-phase reaction. The resulting composite photoanode material was designated as PDI/Cu_2O/Cu. Our findings demonstrate that the synergistic effect between different components of the catalyst significantly increased the activity of PEC CO_2RR. The PDI/Cu_2O/Cu photoanode exhibits a CO yield of approximately 100 μmol/(cm^2·h) at 1.61 V vs. RHE in H-cell. The CO:H_2 ratio can be adjusted by fine-tuning the potential, enabling it to approach the ratio of synthetic gas. At 1.57 V vs. RHE, the CO and H_2 yield rose to 124.47 μmol/(cm^2·h) (CO:H_2 ≈ 1), with the resulting product being the closest match to the syngas ratio. In addition, it is determined by spectral and physical methods that the reason for its high activity is the change of band gap of PDI/Cu_2O/Cu and the improvement of electron transport efficiency. The approach of synthesizing composites to enhance the photoanode and facilitate cathodic reduction reactions offers valuable insight into the potential use of conjugated molecules in the realm of PEC CO_2RR.

2 Experimental section

2.1 Materials

Perylene-3,4,9,10-tetracarboxylic dianhydride (PTCDA, ≥ 98%) was purchased from Beijing InnoChem Science & Technology Co., Ltd. Copper(II) chloride dihydrate ($CuCl_2$·$2H_2O$, ≥ 99%), cupric sulfate ($CuSO_4$, ≥98%) and chloroform ($CHCl_3$, ≥ 99.0%) were obtained from Sinopharm Chemical Reagent Company. Nafion (5 wt.%) solution was purchased from Alfa Aesar. N-(3-Aminopropyl)-imidazole and lactic acid (Ar, ≥ 85%) was bought from Adamas. Potassium hydroxide (KOH, 99.5%) and sodium hydroxide (NaOH, 99.5%) were acquired from Macklin Company. CO_2 gas (99.999%) was purchased from Wuxi Xin Xiyi Technology. Pt mesh (1 cm × 1.5 cm, 0.5 mm thickness) was custom-made from Shanghai Jing Chong Electronic Technology Development Co., Ltd. Silver chloride electrode (Ag/AgCl, CHI111) was purchased from Shanghai Yueci Electronic Technology Co., Ltd. Ultrapure water (18.2 MΩ·cm) was used in this experiment. The size of the Ag sheet is 10 cm × 10 cm, and the thickness is 0.2 mm. The size of the copper sheet is 10 cm × 10 cm, and the thickness is 0.3 mm.

2.2 Characterization

X-ray diffraction (XRD) patterns were collected using a D8 X-ray diffractometer (Bruker AXS, Germany) with a Cu target as a radiation source. The Fourier transform infrared (FT-IR) spectra were recorded on a Nicolet iS50 FT-IR spectrometer (Thermo, USA) with an attenuated total reflectance (ATR) accessory. UV–visible diffuse reflectance spectrascopy (UV–vis DRS) were used on a UV-3600 spectrophotometer (Shimadzu, Japan). Morphologies of the photoanode were obtained by the JEM-2100 transmission electron microscope (TEM) (JEOL, Japan) with an acceleration voltage of 200 kV and S-4800 scanning electron microscope (SEM) (Hitachi, Japan). X-ray photoelectron spectroscopy (XPS) measurements were carried out with an AXIS Supra (Kratos, UK) using monochromatized Al Kα radiation ($h\nu$ = 1486.6 eV, 225 W) as the X-ray source and all spectra were calibrated with C 1s (284.8 eV). The gas phase products were detected by gas chromatography (GC 2060, Shanghai Ruimin Instrument Co., Ltd, China). Steady-state fluorescence (FL) spectra were recorded on an FS5 spectrophotometer (PL, Edinburgh, UK). The Raman spectra were collected on a lab-made Smart Raman confocal-micro-Raman module (a 50× objective len (N.A. = 0.75)) coupled with an iHR550 Raman spectrometer (Horiba, Japan) and a charge-coupled device (CCD) detector.

2.3 Synthesis of perylene tetracarboxylic di-(propyl imidazole) (PDI)

5 g perylene-3,4,9,10-tetracarboxylic dianhydride (PTCDA) and 15 mL N-(3-aminopropyl)-imidazole were mixed with 100 mL N, N-dimethylformamide (DMF) in an argon (Ar) atmosphere. The mixture was then heated to 140 °C for 12 h. After the reaction, the resulting product was washed and filtered with tetrahydrofuran (THF) three times. It was then dried in a vacuum at 60 °C for 8 hours, resulting in a yield of 3.0 g (64.6% yield), which is defined as PDI [19, 20] (Scheme 1).

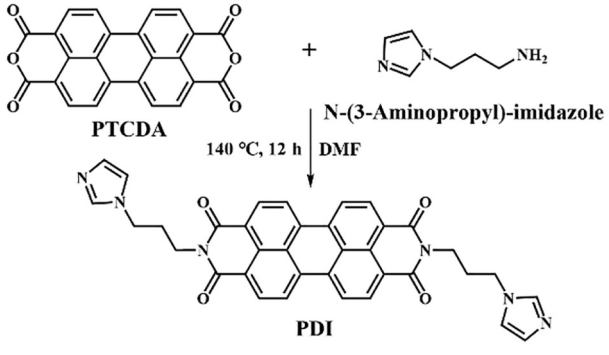

Scheme 1 Schematic diagram of PDI synthesis.

2.4 Synthesis of electrodeposition Cu_2O/Cu

The copper sheet, measuring 2 cm × 2 cm with a thickness of 0.3 mm, underwent polishing to remove any oxide present on the surface. The polished copper sheet was then used as the working electrode for electrodeposition. The electrolyte used consisted of a

mixture of 0.4 M $CuSO_4$ and 3 M lactic acid. The pH of the electrolyte was adjusted to 12 using 3 M NaOH. During the electrodeposition process, a platinum mesh served as the counter electrode, while an Ag/AgCl electrode was used as the reference electrode. Under the applied chronopotentiometry of −1 mA/cm^2, the copper sheet underwent electrodeposition for 3 h. This resulted in the formation of a layer of Cu_2O (brick-red color) on the surface of the copper sheet. The resulting product is then referred to as Cu_2O/Cu [21].

2.5 Synthesis of PDI /Cu_2O/Cu photoanodes

A total of 0.66 g of PDI was added to 50 mL of $CHCl_3$, and the mixture was subjected to ultrasound treatment for 30 min until the PDI was completely dissolved. The resulting solution, which was fluorescent yellow and saturated with PDI, was obtained by filtration. To synthesize PDI/Cu_2O/Cu, the prepared Cu_2O/Cu material was placed in the PDI-saturated solution and heated at 60 °C for 2 h. After cooling, the material was removed from the solution and rinsed with ethanol, resulting in the formation of dark red PDI/Cu_2O/Cu. In addition, we used indium tin oxide (ITO) as the substrate instead of copper sheet and the synthesis steps were the same as those described in Sections 2.4 and 2.5. After drying, the resulting powder scraped from PDI/Cu_2O/ITO can be identified as PDI/Cu_2O.

2.6 PEC CO_2 reduction with three-electrode system

Photoelectrochemical tests were performed in the CHI660e electrochemical workstation with silver as cathode, and Cu_2O/Cu or PDI/Cu_2O/Cu as photoanode. In H-cell, anode and cathode electrolytes are 0.5 M $KHCO_3$ and 1 M KOH, respectively. Nafion 117 is an ion exchange membrane to separates the cathode chamber and anode chamber. For PEC CO_2RR, the working electrode was placed under visible light irradiation (100 mW/cm^2) with different bias voltage, while the cathodic cell was placed in the dark. Before starting the performance test, the cathode chamber needs to be saturated with CO_2 gas and then sealed. After the reaction, the gas composition of the cathode was detected by gas chromatography through injection. The stability experiment of CO_2 reduction is a long-term constant voltage test with PDI/Cu_2O/Cu as the photoanode under visible light irradiation (100 mW/cm^2) at 1.57 V vs. RHE. The gas composition of the cathode chamber was detected every 1 h.

2.7 Electrochemical and photoelectrochemical measurements

Photoelectrochemical measurements used the electrochemical workstation (CHI750e) and visible light (300 W Xe lamp, Beijing, China). In a typical three-electrode system, Nafion 117, Pt mesh and saturated Ag/AgCl were used as cation exchange membrane, counter electrode and reference electrode, respectively. In the transient photocurrent, linear sweep voltammetry (LSV) and electrochemical impedance spectroscopy (EIS) tests, 0.5 M $KHCO_3$ was used as the cathode electrolyte and 1 M KOH was used as the anode electrolyte. The open-circuit potential was measured with 0.1 M Na_2SO_4 as the electrolyte. The electrode potential of the working electrode is converted to the reversible hydrogen electrode (RHE) potential by the Nernst equation in this work. All performance data were corrected with an *iR* compensation of 80% [22].

Nernst equation:

$$E_{RHE}\ (V) = E_{Ag/AgCl}\ (V) + 0.210\ V + 0.059\ V \times pH - 80\% \times i \times R$$

3 Results and discussion

Figure 1(a) illustrates the setup of our PEC CO_2RR system. The photoanode is a granular metal-organic framework (MOF) structure grown on the surface of Cu_2O film. In the mixed solution of $CuSO_4$ and lactic acid, a layer of Cu_2O film is electrodeposited on the copper substrate as a copper precursor [21]. Then, PDI was grown on the surface of the Cu_2O thin film via a solid phase reaction (Fig. S1 in the Electronic Supplementary Material (ESM)). Compared with pure Cu_2O and PDI (Fig. 1(b) and Fig. S2 in the ESM), the slight positive shift in all XRD peaks of PDI/Cu_2O indicates a reduction in lattice distances [23]. The presence of PDI leads to a notable decrease in peak intensity on the (200) crystal face of Cu_2O. The yellow area indicates that the crystalline PDI is turned into amorphous PDI due to the solid phase reaction.

Examining the interface between Cu_2O and PDI is also crucial. TEM image (Fig. 1(c)) shows that the material has well-defined crystal boundaries and the exposed lattice fringes are the (111) crystal faces of Cu_2O [23, 24]. According to SEM image of pure Cu_2O and TEM images of Cu_2O and PDI/Cu_2O in Fig. S3 in the ESM, the outer layer in Fig. 1(c) is the amorphous PDI. Cross-section SEM image (Fig. 1(d)) shows that PDI is a prominent particle structure growing from the surface of Cu_2O. The average thickness is 0.5 μm.

To study the interaction between copper ions and PDI, FT-IR spectroscopy and Raman spectroscopy were performed for Cu_2O, PDI, and PDI/Cu_2O photoanodes to determine the change of chemical bond formed by solid phase reaction. By FT-IR spectral analysis (Fig. 2(a)), the peaks at 1685.0 and 1645.0 cm^{-1} belong to in-plane (asymmetric) and out-of-plane (symmetric) –C=O stretching, respectively, which proves the presence of imine bonds. The peaks at 1590.5 and 1337.9 cm^{-1} are attributed to the stretching vibration of C=C and C–N–C absorption of the imidazole ring, respectively. 1574.6 cm^{-1} is the absorption peak of the bending vibration of N–H [25]. In addition, Cu–N bonding absorption peaks at 745.8 and 726.6 cm^{-1} can be observed in the FT-IR spectrum of PDI/Cu_2O [26].

Raman spectra (Fig. 2(b)) show that PDI/Cu_2O can detect not only the characteristic peak of PDI (yellow region) but also the characteristic peak of the Cu–O bond of Cu_2O (purple region) [23, 27]. Hence, we postulate that a coordination bond between Cu in the Cu_2O and O in the PDI could potentially be established. The peak of Cu_2O near 600 cm^{-1} coincides with the peak of PDI. The results of combining infrared data show that a hybrid structure composed of two materials Cu_2O and PDI is formed on the photoanode and there may be two coordination forms of Cu–N and Cu–O.

As shown in Fig. 2(c), the fitted peaks of 952.98 and 933.08 eV belong to $2p_{1/2}$ and $2p_{3/2}$ of Cu^{2+}, while the peaks of 951.78 and 931.88 eV belong to $2p_{1/2}$ and $2p_{3/2}$ of Cu^{+}, respectively. So it can be concluded that XPS Cu 2p spectra of Cu_2O and PDI/Cu_2O contain Cu^{+} and Cu^{2+}. According to the content percentage of different valence states of copper atoms in the samples listed in Table S1 (obtained by fitting by Case XPS software) in the ESM, the content of Cu^{2+} in PDI/Cu_2O (42.97%) was significantly higher than that in Cu_2O (27.91%). It is well known that Cu LMM XPS spectra are generally used to distinguish between Cu^{+} and Cu^{0}. XPS Cu LMM

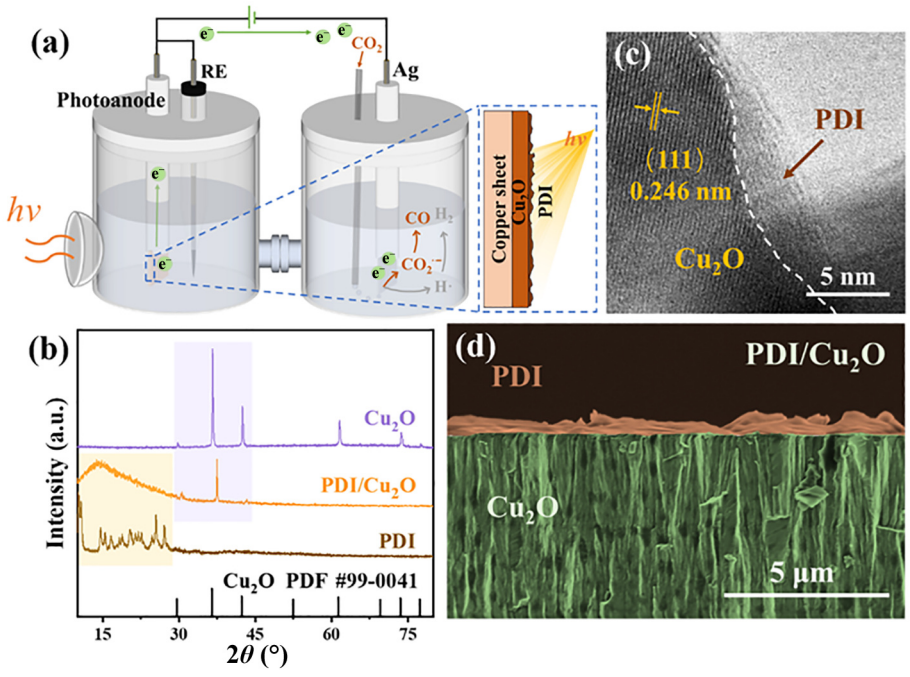

Figure 1 (a) Schematic illustration for PEC CO_2RR using a PDI/Cu_2O/Cu photoanode. (b) XRD patterns of Cu_2O, PDI and PDI/Cu_2O. (c) High-resolution TEM image and (d) cross-section SEM image of PDI/Cu_2O.

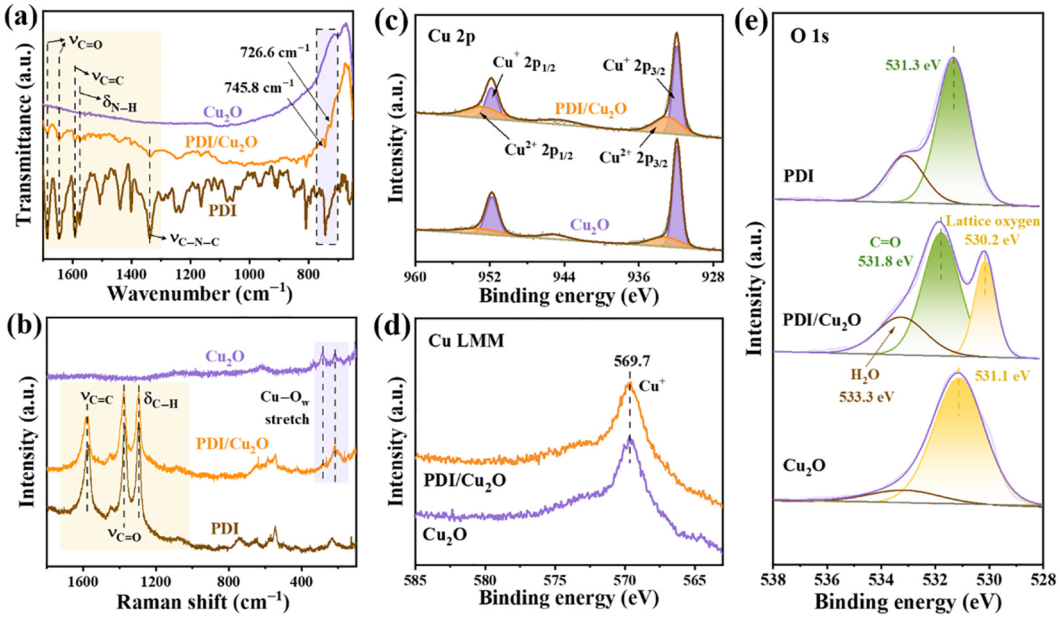

Figure 2 (a) FT-IR and (b) Raman spectra of Cu_2O, PDI and PDI/Cu_2O. (c) XPS Cu 2p spectra of PDI/Cu_2O and Cu_2O; (d) XPS Cu LMM spectra of Cu_2O and PDI/Cu_2O; (e) XPS O 1s spectra of PDI/Cu_2O, Cu_2O and PDI.

spectra in Fig. 2(d) show its peak in 569.7 eV, and we attribute it to Cu^+. However, there is no Cu^0 peak near 568 eV, which proves that there is no Cu^0 in the materials. Combined with XPS Cu 2p spectra, it is proved that Cu_2O and PDI/Cu_2O are composed of Cu^+ and Cu^{2+}.

The XPS O 1s spectrum fitting peaks of PDI/Cu_2O in Fig. 2(e) are located at 533.3, 531.8 and 530.2 eV, respectively, which belong to the characteristic peaks of H_2O, C=O and Cu–O lattice oxygen [28, 29]. Compared with the shift of PDI and Cu_2O, C=O peaks to the direction of large binding energy, the lattice oxygen peak of Cu–O shifts to the direction of lower binding energy, so the electron cloud density on C=O decreases and the electron cloud density on lattice oxygen increases.

The fitting peaks in the XPS N 1s spectrum of PDI/Cu_2O in Fig. S4 in the ESM are located at 401.3, 400.5 and 398.9 eV respectively, corresponding to the characteristic peaks of graphite N, pyrrolidine N and C–N=C, respectively [20]. Compared with PDI, the peak averages of pyrrolidine N and C–N=C move to a larger position of binding energy, so the electron cloud density on N decreases. Combined with the O 1s spectra, the electron cloud density of C=O in the PDI and N on the imidazole ring decreases, while the electron cloud density of O in the Cu_2O structure increases. It is

proved that the PDI/Cu_2O electrons formed after the reaction are transferred from the conjugated large π bond of PDI to Cu_2O and enriched on Cu_2O.

Apart from possessing outstanding PEC water oxidation photoanode catalysts, the selection of an ideal cathode catalyst with high activity and selectivity is crucial for the conversion of CO_2 into syngas. In Fig. S5 in the ESM, the activity and selectivity of CO products of different cathode catalysts were tested at the potential of 1.9 V vs. RHE using Pt as the anode. Among various Ag-based cathode materials, the activity of Ag foil is much higher than that of Ag/Sn, Ag/Pd, and Ag NPs, nearly twice as much as that of p-Ag and Ag NNs. Accordingly, an Ag foil catalyst was selected as the cathode for integration with PDI/Cu_2O photoanode to construct PEC CO_2 reduction systems. Figure S6 in the ESM filters the photoanode substrate, electrodeposition Cu_2O optimal time, and PDI growth time, further optimizing the PEC water oxidation photoanode half-reaction. The final choice is to use the copper sheet as the base. Cu_2O film was formed by electrodeposition with a constant current of −1 mA/cm^2 for 3 h, and photoanode was synthesized by solid phase reaction in PDI saturated solution for 2 h.

In Fig. 3(a), the PEC CO_2RR performance of PDI/Cu_2O/Cu, Cu_2O/Cu, and Cu as photoanodes in H-cell was tested respectively. With the increase of applied voltage, the CO yield is also gradually increasing. In the dark, when PDI/Cu_2O/Cu is used as the anode, the CO yield is significantly higher than that of Cu_2O/Cu. When the cathodic conditions are the same, the main way for the anode to influence the cathodic reaction is through the transmission and utilization of electrons. A more efficient anodic reaction can suppress excessive charge accumulation and facilitate selective CO_2 reduction at the cathode. This provides evidence that the PDI/Cu_2O/Cu anode is capable of contributing a greater quantity of electrons to the CO_2 reduction at the cathode. In the light, the CO yield of PDI/Cu_2O/Cu was significantly increased by 2 times at 1.57 V vs. RHE. This observation once again verified that photogenerated electrons on PDI and Cu_2O can be preferentially transferred to the cathode, thus enhancing the reduction effect of the cathode. Notably, the minimum potential required for CO_2 reduction when PDI/Cu_2O/Cu was used as the photoanode was lower than the other experimental conditions and exhibited higher performance than the others in all potentials. In addition, after illumination, both PDI/Cu_2O/Cu and Cu_2O/Cu as anode showed a substantial improvement relative to the dark condition. In contrast, there is almost no change when Cu is used as the photoanode, which is because Cu itself cannot oxidize water, and thus almost no CO_2 reduction products can be generated in the system with Cu as the anode. Figure 3(b) is the LSV of PDI/Cu_2O/Cu and Cu_2O/Cu in the dark and light. When the potential of the photoanode reaches the initial potential of the OER reaction, the current density increases sharply, and the change of current density under PDI/Cu_2O/Cu-light is the fastest. The initial potential of PDI/Cu_2O/Cu photoanode is 1.5 V vs. RHE, while the current density increases sharply at 1.55 V vs. RHE. It is well known that high current density tends to lead to high CO yield, which is consistent with the test results in Fig. 3(a) (the abrupt change in CO yield at 1.55 V vs. RHE). The current density of 1h of PDI/Cu_2O/Cu under visible light irradiation at different applied potentials is shown in Fig. S7 in the ESM. Compared to 1.49 and 1.54 V vs. RHE, the current density of 1.55 V vs. RHE greatly increases.

More importantly, by changing the bias potential of the PDI/Cu_2O/Cu photoanode, the CO selectivity is reasonably adjusted from 13.9% to 56.3%, closer to the ratio of syngas (Fig. 3(c)). However, The CO selectivity of PDI/Cu_2O/Cu in the dark can reach 47.0%, which is close to the ratio of syngas, but the CO yield is far lower than that under visible light irradiation. On the contrary, when Cu_2O is used as the anode, the hydrogen evolution side reaction is dominant, leading to a CO selectivity of less than 30% whether under dark or visible light irradiation (Fig. S8 in the ESM). In addition, in conventional electrocatalytic CO_2 reduction systems, Pt is usually used as the anode. For comparison, we tested the CO_2RR performance with Pt as anode and Ag foil as cathode (Fig. S9 in the ESM). Because of the poor OER activity of the Pt catalyst, the CO_2RR activity of Pt as anode is not as good as that of the PDI/Cu_2O/Cu catalyst.

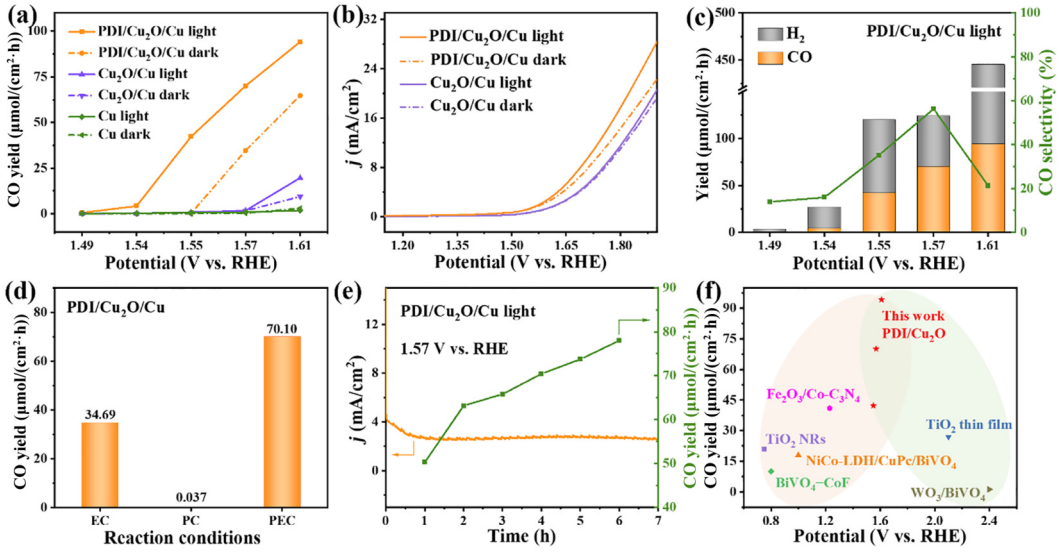

Figure 3 (a) Yields of CO under visible light irradiation and in the dark using Cu, Cu_2O/Cu, and PDI/Cu_2O/Cu as the photoanode. (b) LSV of PDI/Cu_2O/Cu and Cu_2O/Cu in the dark and light. (c) Production yields and CO selectivity of PDI/Cu_2O/Cu under visible light irradiation at different applied potentials. (d) CO yield for EC, PC, and PEC CO_2RR of PDI/Cu_2O/Cu. (e) The CO production amounts and current density on PDI/Cu_2O/Cu photoanode at 1.57 V vs. RHE. (f) Comparison of CO yield on different photoanodes.

To prove that the PEC CO_2RR is not a simple addition of photocatalytic (PC) and electrocatalytic (EC) reactions, we test the CO yields of PDI/Cu_2O/Cu under PC, EC, and PEC CO_2RR conditions respectively (Fig. 3(d)). The CO yield of PC CO_2RR with PDI/Cu_2O/Cu as anode is 0.037 μmol/(cm^2·h). The CO yield of EC CO_2RR is 34.69 μmol/(cm^2·h) at 1.57 V vs. RHE. Surprisingly, the CO yield reached 70.10 μmol/(cm^2·h) in the PEC CO_2RR. Therefore, in the process of the PEC system, the synergistic effect of applied potential and irradiation can be well reflected. The apparent high PEC CO_2RR activity and selectivity are not the result of pure EC or PC processes [30, 31]. In addition, we tested the cumulative CO production of PDI/Cu_2O/Cu for 6 h and the current density curve at 1.57 V vs. RHE (Fig. 3(e)) to verify the durability of the photoanode. The continuous and steady growth of CO and the change of current density are negligible, indicating that PDI/Cu_2O/Cu has good stability. Figure 3(f) and Table S2 in the ESM show the comparison of the photoelectrochemical performance of CO_2 in the photoanode system previously reported [32–37]. This work can obtain better performance at a moderate potential. The Ag foil cathode was integrated with the PDI/Cu_2O/Cu photoanode to convert CO_2 to syngas in a typical three-electrode system with yields up to 124.47 μmol/(cm^2·h) (yields of CO and H_2). Under the potential of 1.61 V vs. RHE, the CO yield of PEC CO_2RR in H-cell reached nearly 100 μmol/(cm^2·h). Some materials previously reported in the literature, such as TiO_2 thin film and WO_3/$BiVO_4$ as a photoanode, require a larger overpotential to achieve a higher CO yield (green zone), and some can be achieved at a lower potential (pink zone). However, their CO yield is significantly lower than that of this work.

To gain insight into the underlying mechanism of PDI promotion, a series of characterizations were performed. UV–vis DRS spectra (Fig. 4(a)) show that the absorbance edge of pure Cu_2O is at 652 nm [38], while the absorbance edge of PDI/Cu_2O is significantly improved and slightly redshifted. Calculated from the Tauc plot (inset in Fig. 4(a)), the band gap energy of PDI/Cu_2O is slightly reduced to 1.91 eV compared to that before PDI loading (1.94 eV). This is due to the alteration of the band structure resulting from the solid-phase reaction between Cu atoms and PDI, which replaces the Cu_2O lattice. This change facilitates more efficient use of visible light, increasing PEC CO_2RR activity.

In the Bode phase plot (Fig. 4(b)), the electron lifetime (t) can be estimated using the equation $t = 1/(2\pi f_p)$, where f_p is the peak frequency corresponding to the charger transfer process at the photoanode/electrolyte interface [39]. The introduction of PDI significantly prolongs the electronic life of the photoanode. The electron lifetime is more than twice from 73.57 ms for Cu_2O to 186.74 ms for PDI/Cu_2O/Cu [40]. The increase in electron lifetime is due to the reduction of the electron and hole recombination process, which accelerates electron transport and increases the electron density, which further leads to improved device performance. It is consistent with the result analysis of EIS in Fig. S10 in the ESM.

Photoluminescence (PL) spectrascopy is one of the useful techniques to observe the efficiency of carrier separation in semiconductors [41]. PL emission spectra of Cu_2O and PDI/Cu_2O were recorded at the excitation wavelength of 405 nm. Pure Cu_2O has a strong ultraviolet emission peak at 653 nm and a weak ultraviolet emission peak at 717 nm (Fig. 4(c)) [42]. Compared with pure Cu_2O, the PL emission peak intensity of PDI/Cu_2O is reduced. A lower PL intensity generally implies a lower electron-hole recombination rate. This indicates that the carrier separation efficiency of PDI/Cu_2O is higher, while most of the photogenerated electrons are captured by the catalyst.

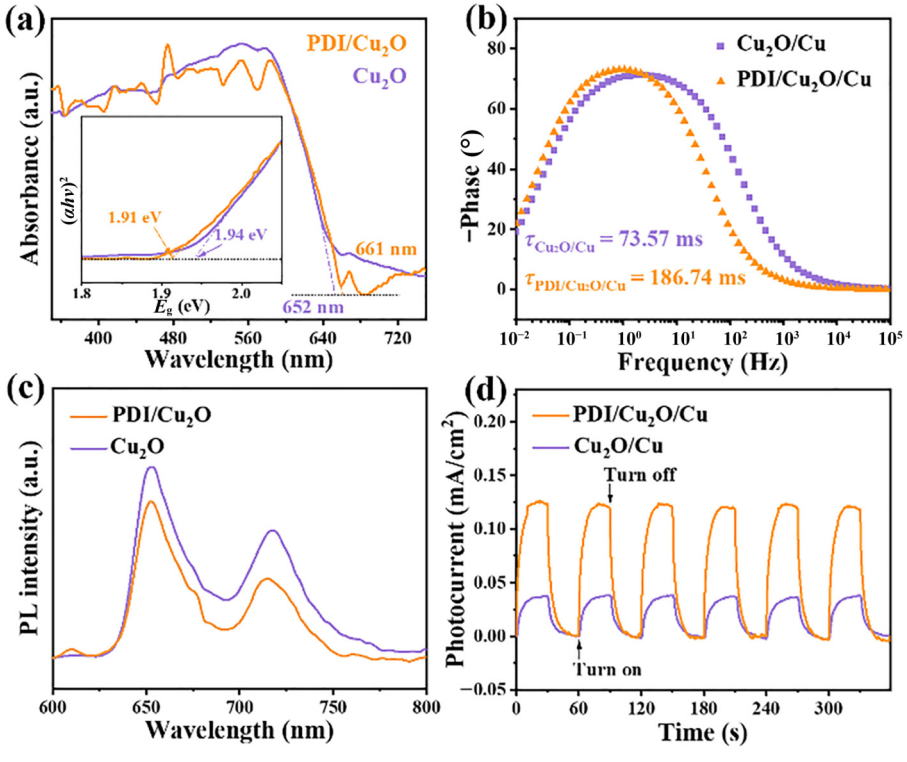

Figure 4 (a) UV–vis DRS spectra of Cu_2O and PDI/Cu_2O. Inset is the concurrent Tauc-plot for the band gap determination. (b) Bode phase plot of Cu_2O/Cu and PDI/Cu_2O/Cu under visible light irradiation and in the dark. (c) Photoluminescence spectra of Cu_2O and PDI/Cu_2O. (d) The transient photocurrent density of Cu_2O/Cu and PDI/Cu_2O/Cu.

The internal electric field strength can be reflected by the open circuit potentials [26]. It is shown in Fig. S11 in the ESM that the open-circuit potentials of PDI/Cu_2O and Cu_2O are 0.13 and 0.06 V, respectively. Therefore, the internal electric field of PDI/Cu_2O is 2.17 times that of Cu_2O. Furthermore, to demonstrate the material's photo response, the photocurrents of PDI/Cu_2O/Cu and Cu_2O/Cu were measured at 1.57 V vs. RHE (Fig. 4(d)). With the addition of PDI, the photocurrent was significantly enhanced, reaching approximately 3 times that of Cu_2O. This suggests that PDI/Cu_2O/Cu exhibits improved photoelectron and hole transfer efficiency. The observed changes in the band gap, as well as the results from PL and electrochemical test analyses, indicate that the introduction of PDI enhances the separation efficiency of photogenerated carriers. As a result, the current density in the system increases, leading to improved performance in PEC CO_2RR.

The PDI molecule possesses a narrow band gap and high band edge oxidation potential, making it a superior photocatalyst with excellent photocatalytic activity. By growing PDI on the electrodeposited Cu_2O surface, the charge transfer rate on the catalyst surface is effectively enhanced, reducing electron–hole recombination and prolonging the electron lifetime. This results in increased electron density at the cathode. Figure 5 presents a schematic diagram illustrating the PEC CO_2RR on the PDI/Cu_2O/Cu photoanode. PDI facilitates a reduction in the electron transition band gap, making the catalyst more responsive to visible light irradiation and promoting the anodization reaction. It is easier for photogenerated electrons to jump from the valence band transfer to the surface, and quickly transfer to the cathode through the external circuit, where CO_2 is gathered and effectively converted into CO. At the same time, the hole in the valence band can enhance the anodic oxidation reaction and further promote cathodic CO_2 reduction.

4 Conclusions

In summary, we conducted an electrodeposition of a 5–10 μm-thick layer of Cu_2O on a Cu sheet substrate. This was followed by a solid-phase reaction to grow PDI on the Cu_2O/Cu surface. The PDI/Cu_2O/Cu photoanode catalyst exhibited enhanced water oxidation activity in the presence of visible light. It facilitated the rapid extraction of photogenerated holes, allowing the separated electrons to move toward the cathode under the applied potential. This, in turn, assisted the CO_2RR at the cathode. Under visible light irradiation at 1.61 V vs. RHE, the PDI/Cu_2O/Cu catalyst achieved a CO yield of nearly 100 μmol/(cm²·h). Furthermore, the syngas yield reached 124.47 μmol/(cm²·h) with a ratio of CO to H_2 that can be adjusted by manipulating the potential. Controlling the CO/H_2 ratio enables better optimization of feedstock composition for targeted hydrocarbon production, reducing the need for additional gas separation or conditioning steps [43–45]. To investigate the underlying mechanism of PDI promotion, we utilized Tauc-plot and Bode phase plot analyses. They revealed changes in the energy band structure of the PDI/Cu_2O/Cu catalyst after the solid-phase reaction. These changes improved the utilization of visible light and prolonged the electron lifetime after carrier separation. The high CO_2 reduction activity of PDI/Cu_2O/Cu catalyst is mainly because the introduction of PDI reduces the band gap of the photoanode, improves the separation efficiency of electrons and holes, and promotes the electron enrichment of the cathode. The strategy of improving photoanode to promote cathodic reduction reaction through synergistic interaction between different components of organic and inorganic phases provides insight for the construction of a high-performance CO_2 reduction system in the future.

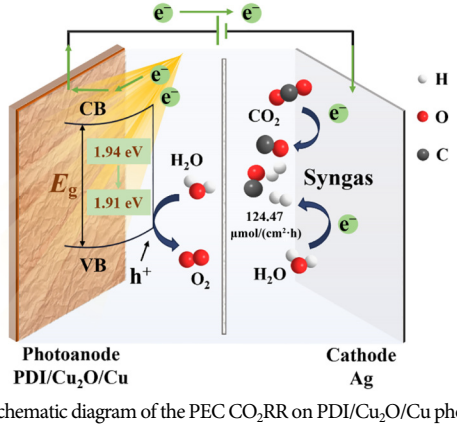

Figure 5 Schematic diagram of the PEC CO_2RR on PDI/Cu_2O/Cu photoanode.

Electronic Supplementary Material: Supplementary material (SEM, XRD, XPS characterizations and detailed electrochemical measurements of PDI/Cu_2O/Cu, PDI/Cu_2O and Cu_2O catalysts) is available in the online version of this article at https://doi.org/10.26599/NR.2025.94907306.

Data availability

All data needed to support the conclusions in the paper are presented in the manuscript and the ESM. Additional data related to this paper may be requested from the corresponding author upon request.

Acknowledgements

This work was supported by the National Natural Science Foundation of China (No. 22379054) and Startup Funding at Jiangnan University.

Author contribution statement

C. C. Z. designed and carried out the experiments, analyzed data and wrote the draft. C. F. C. performed the UV–vis DRS spectra. J. J. M. performed the XRD measurements. D. W. and P. L. provided experimental guidance on photoelectrochemical carbon dioxide reduction. Q. Q. S. and Y. M. X. participated in the discussion and revision of the draft. Y. Z. (Ying Zhang), Y. Z. (Yong Zhao), Y. W., and Y. F. Z. provided resources, directed research efforts, and reviewed and revised the manuscript.

Declaration of competing interest

All the contributing authors report no conflict of interests in this work.

Use of AI statement

None.

References

[1] Zhang, Y. D.; Sun, Y. J.; Wang, Q. Y.; Zhuang, Z. C.; Ma, Z. T.; Liu, L. M.; Wang, G. M.; Wang, D. S.; Zheng, X. S. Synergy of photogenerated electrons and holes toward efficient photocatalytic

urea synthesis from CO_2 and N_2. *Angew. Chem., Int. Ed.* **2024**, *63*, e202405637.

[2] Ning, S. B.; Ou, H. H.; Li, Y. G.; Lv, C. C.; Wang, S. F.; Wang, D. S.; Ye, J. H. Co^0–$Co^{\delta+}$ interface double-site-mediated C–C coupling for the photothermal conversion of CO_2 into light olefins. *Angew. Chem., Int. Ed.* **2023**, *62*, e202302253.

[3] Jiang, Z. N.; Ren, S.; Cao, X.; Fan, Q. K.; Yu, R.; Yang, J.; Mao, J. J. pH-universal electrocatalytic CO_2 reduction with ampere-level current density on doping-engineered bismuth sulfide. *Angew. Chem. , Int. Ed.* **2024**, *63*, e202408412.

[4] Zhang, M. Y.; Zhou, D. Y.; Mu, X. Q.; Wang, D. S.; Liu, S. L.; Dai, Z. H. Regulating the critical intermediates of dual-atom catalysts for CO_2 electroreduction. *Small* **2024**, *20*, 2402050.

[5] Chen, S. H.; Zheng, X. B.; Zhu, P.; Li, Y. P.; Zhuang, Z. C.; Wu, H. J.; Zhu, J. X.; Xiao, C. H.; Chen, M. Z.; Wang, P. S. et al. Copper atom pairs stabilize *OCCO dipole toward highly selective CO_2 electroreduction to C_2H_4. *Angew. Chem., Int. Ed.* **2024**, *63*, e202411591.

[6] Ma, F. Y.; Zhang, P. F.; Zheng, X. B.; Chen, L.; Li, Y. R.; Zhuang, Z. C.; Fan, Y. M.; Jiang, P.; Zhao, H.; Zhang, J. W. et al. Steering the site distance of atomic Cu–Cu pairs by first-shell halogen coordination boosts CO_2-to-C_2 selectivity. *Angew. Chem., Int. Ed.* **2024**, *63*, e202412785.

[7] Tao, Y.; Guan, J. P.; Zhang, J.; Hu, S. Y.; Ma, R. Z.; Zheng, H. R.; Gong, J. X.; Zhuang, Z. C.; Liu, S. J.; Ou, H. H. et al. Ruthenium single atomic sites surrounding the support pit with exceptional photocatalytic activity. *Angew. Chem., Int. Ed.* **2024**, *63*, e202400625.

[8] Pan, W. Y.; Wei, Z. H.; Su, Y. H.; Lian, Y. B.; Zheng, Z. Y.; Yuan, H. H.; Qin, Y. Z.; Xie, X. L.; Bai, Q. Q.; Jiao, Z. Y. et al. Hydroxylated metal-organic-layer nanocages anchoring single atomic cobalt sites for robust photocatalytic CO_2 reduction. *Nano Res.* **2024**, *17*, 2410–2419.

[9] Wang, G.; Wu, Y.; Li, Z. J.; Lou, Z. Z.; Chen, Q. Q.; Li, Y. F.; Wang, D. S.; Mao, J. J. Engineering a copper single-atom electron bridge to achieve efficient photocatalytic CO_2 conversion. *Angew. Chem., Int. Ed.* **2023**, *62*, e202218460.

[10] Fang, J. J.; Zhu, C. Y.; Hu, H. L.; Li, J. Q.; Li, L. C.; Zhu, H. Y.; Mao, J. J. Progress of photocatalytic CO_2 reduction toward multi-carbon products. *Sci. China Chem.* **2024**, *67*, 3994–4013.

[11] Abdi, F. F.; van de Krol, R. Nature and light dependence of bulk recombination in Co–Pi-catalyzed $BiVO_4$ photoanodes. *J. Phys. Chem. C* **2012**, *116*, 9398–9404.

[12] Chang, X. X.; Wang, T.; Zhang, P.; Zhang, J. J.; Li, A.; Gong, J. L. Enhanced surface reaction kinetics and charge separation of p–n heterojunction Co_3O_4/$BiVO_4$ photoanodes. *J. Am. Chem. Soc.* **2015**, *137*, 8356–8359.

[13] Wang, Y.; Ma, F. Y.; Zhang, G. Q.; Zhang, J. W.; Zhao, H.; Dong, Y. M.; Wang, D. S. Precise synthesis of dual atom sites for electrocatalysis. *Nano Res.* **2024**, *17*, 9397–9427.

[14] Gan, T.; Wang, D. S. Atomically dispersed materials: Ideal catalysts in atomic era. *Nano Res.* **2024**, *17*, 18–38.

[15] Wang, L. Q.; Si, W. P.; Hou, X. G.; Wang, M. X.; Liu, X. L.; Ye, Y. H.; Hou, F.; Liang, J. Novel integrated strategies toward efficient and stable unassisted photoelectrochemical water splitting. *Sustain. Mater. Technol.* **2020**, *25*, e00209.

[16] Wang, J.; Liu, D.; Zhu, Y. F.; Zhou, S. Y.; Guan, S. Y. Supramolecular packing dominant photocatalytic oxidation and anticancer performance of PDI. *Appl. Catal. B: Environ.* **2018**, *231*, 251–261.

[17] Yang, J.; Miao, H.; Li, W. L.; Li, H. Q.; Zhu, Y. F. Designed synthesis of a p-Ag_2S/n-PDI self-assembled supramolecular heterojunction for enhanced full-spectrum photocatalytic activity. *J. Mater. Chem. A* **2019**, *7*, 6482–6490.

[18] Ghosh, S.; Kouamé, N. A.; Ramos, L.; Remita, S.; Dazzi, A.; Deniset-Besseau, A.; Beaunier, P.; Goubard, F.; Aubert, P. H.; Remita, H. Conducting polymer nanostructures for photocatalysis under visible light. *Nat. Mater.* **2015**, *14*, 505–511.

[19] Gui, J. N.; Li, L. B.; Yu, B. Y.; Wang, D.; Yang, B.; Gu, Q. Q.; Zhao, Y.; Zhu, Y. F.; Zhang, Y. Modulation of the coordination environment of copper for stable CO_2 electroreduction with tunable selectivity. *ACS Appl. Mater. Interfaces* **2023**, *15*, 25516–25523.

[20] Zhang, Y.; Zhang, C. C.; Wang, D.; Gui, J. N.; Mao, J. J.; Lou, Y.; Pan, C. S.; Zhu, Y. F. *In situ* formed copper nanoparticles via strong electronic interaction with organic skeleton for pH-universal electrocatalytic CO_2 reduction. *J. Mater. Chem. A* **2023**, *11*, 22992–23000.

[21] Liu, G. J.; Zheng, F.; Li, J. R.; Zeng, G. S.; Ye, Y. F.; Larson, D. M.; Yano, J.; Crumlin, E. J.; Ager, J. W.; Wang, L. W. et al. Investigation and mitigation of degradation mechanisms in Cu_2O photoelectrodes for CO_2 reduction to ethylene. *Nat. Energy* **2021**, *6*, 1124–1132.

[22] Ren, W. H.; Tan, X.; Qu, J. T.; Li, S. S.; Li, J. T.; Liu, X.; Ringer, S. P.; Cairney, J. M.; Wang, K. X.; Smith, S. C. et al. Isolated copper-tin atomic interfaces tuning electrocatalytic CO_2 conversion. *Nat. Commun.* **2021**, *12*, 1449.

[23] Zhou, Y. X.; Yao, Y. B.; Zhao, R.; Wang, X. X.; Fu, Z. Z.; Wang, D. W.; Wang, H. Z.; Zhao, L.; Ni, W.; Yang, Z. Y. et al. Stabilization of Cu^+ via strong electronic interaction for selective and stable CO_2 electroreduction. *Angew. Chem., Int. Ed.* **2022**, *61*, e202205832.

[24] Zhou, Q. Q.; Chen, Y. X.; Shi, H. Y.; Chen, R.; Ji, M. H.; Li, K. X.; Wang, H. L.; Jiang, X.; Lu, C. Z. The construction of p/n-Cu_2O heterojunction catalysts for efficient CO_2 photoelectric reduction. *Catalysts* **2023**, *13*, 857.

[25] Zhang, T.; Wu, J. D.; Wang, Z.; Wei, Z.; Liu, J. H.; Gong, X. Z. Transfer of molecular oxygen and electrons improved by the regulation of C–N/C=O for highly efficient 2e-ORR. *Chem. Eng. J.* **2022**, *433*, 133591.

[26] Deng, X.; Li, R.; Wu, S. K.; Wang, L.; Hu, J. H.; Ma, J.; Jiang, W. B.; Zhang, N.; Zheng, X. S.; Gao, C. et al. Metal-organic framework coating enhances the performance of Cu_2O in photoelectrochemical CO_2 reduction. *J. Am. Chem. Soc.* **2019**, *141*, 10924–10929.

[27] Zhang, Y. N.; Wang, D.; Liu, W. X.; Lou, Y.; Zhang, Y.; Dong, Y. M.; Xu, J.; Pan, C. S.; Zhu, Y. F. Create a strong internal electric-field on PDI photocatalysts for boosting phenols degradation via preferentially exposing π-conjugated planes up to 100%. *Appl. Catal. B: Environ.* **2022**, *300*, 120762.

[28] Guan, L. L.; Shu, Y.; Jiang, Y. H.; Zhao, F.; Wei, Y. B.; Yan, J. C.; Ren, Y.; Zhou, X. W.; Liu, Z. Rational design and fabrication of Cu_2O film as photoelectrode for water splitting. *J. Alloy. Compd.* **2023**, *956*, 170283.

[29] Zhang, Y. H.; Lee, S.; Jeong, S.; Son, E.; Baik, J. M.; Han, Y. K.; Park, H. Phase-bridged hierarchical catalysts for efficient and stable water electrolysis. *Adv. Funct. Mater.* **2024**, *34*, 2309250.

[30] Yi, X. S.; Zhang, S. Q.; Shen, H.; Li, B.; Yang, L. X.; Dai, W. L.; Song, R. J.; Zou, J. P.; Luo, S. L. Atomic sulfur dissimilation remolding $ZnIn_2S_4$ nanosheets surface to enhance built-internal electric field for photocatalytic CO_2 conversion to syngas. *Appl. Catal. B: Environ.* **2023**, *338*, 123003.

[31] Akbar, M. B.; Wang, Y. J.; Zhang, X. H.; He, T. Study on photoelectrochemical CO_2 reduction over Cu_2O. *J. Photochem. Photobiol. A: Chem.* **2023**, *437*, 114483.

[32] Zhao, B.; Huang, X. J.; Ding, Y.; Bi, Y. P. Bias-free solar-driven syngas production: A Fe_2O_3 photoanode featuring single-atom cobalt integrated with a silver-palladium cathode. *Angew. Chem., Int. Ed.* **2023**, *62*, e202213067.

[33] Chang, X. X.; Wang, T.; Zhang, P.; Wei, Y. J.; Zhao, J. B.; Gong, J. L. Stable aqueous photoelectrochemical CO_2 reduction by a Cu_2O dark cathode with improved selectivity for carbonaceous products. *Angew. Chem., Int. Ed.* **2016**, *55*, 8840–8845.

[34] Wang, T. X.; Guo, L. L.; Pei, H.; Chen, S. T.; Li, R. J.; Zhang, J.; Peng, T. Y. Electron-rich pincer ligand-coupled cobalt porphyrin polymer with single-atom sites for efficient (photo)electrocatalytic CO_2 reduction at ultralow overpotential. *Small* **2021**, *17*, 2102957.

[35] Wang, D.; He, Y. N.; Zhong, N.; He, Z. Q.; Shen, Y.; Zeng, T.; Lu, X. H.; Ma, J.; Song, S. *In situ* chloride-mediated synthesis of TiO_2 thin film photoanode with enhanced photoelectrochemical activity for carbamazepine oxidation coupled with simultaneous cathodic H_2 production and CO_2 conversion to fuels. *J. Hazard. Mater.* **2021**, *410*, 124563.

[36] Wang, Y.; Zhu, Y.; Sun, L. C.; Li, F. Selective CO production by photoelectrochemical CO_2 reduction in an aqueous solution with cobalt-based molecular redox catalysts. *ACS Appl. Mater. Interfaces* **2020**, *12*, 41644–41648.

[37] Lu, W. W.; Zhang, Y.; Zhang, J. J.; Xu, P. Reduction of gas CO_2 to CO with high selectivity by Ag nanocube-based membrane cathodes in a photoelectrochemical system. *Ind. Eng. Chem. Res.* **2020**, *59*, 5536–5545.

[38] Xu, L.; Zhang, F. Y.; Song, X. Y.; Yin, Z. L.; Bu, Y. X. Construction of reduced graphene oxide-supported Ag–Cu_2O composites with hierarchical structures for enhanced photocatalytic activities and recyclability. *J. Mater. Chem. A* **2015**, *3*, 5923–5933.

[39] Chen, X. B.; Tang, Y.; Liu, W. W. Efficient dye-sensitized solar cells based on nanoflower-like ZnO photoelectrode. *Molecules* **2017**, *22*, 1284.

[40] Yang, M.; Zhao, X. Y.; Ma, L. Q.; Yao, Y.; Ding, Y.; Shen, X. D. Electrochemical properties of Cu_2O/Cu composite particles prepared by a novel and facile method. *Electrochim. Acta* **2011**, *56*, 5783–5787.

[41] Udayabhanu; Nagaraju, G.; Nagabhushana, H.; Suresh, D.; Anupama, C.; Raghu, G. K.; Sharma, S. C. *Vitis labruska* skin extract assisted green synthesis of ZnO super structures for multifunctional applications. *Ceram. Int.* **2017**, *43*, 11656–11667.

[42] Basavalingaiah, K. R.; Harishkumar, S.; Nagaraju, G. Synthesis of Cu_2O/Ag composite nanocubes with promising photoluminescence and photodegradation activity over methylene blue dye. *Adv. Mater. Lett.* **2019**, *10*, 832–838.

[43] Zhang, Y.; Mu, X. Q.; Liu, Z. Y.; Zhao, H. Y.; Zhuang, Z. C.; Zhang, Y. F.; Mu, S. C.; Liu, S. L.; Wang, D. S.; Dai, Z. H. Twin-distortion modulated ultra-low coordination PtRuNi-O_x catalyst for enhanced hydrogen production from chemical wastewater. *Nat. Commun.* **2024**, *15*, 10149.

[44] Mu, X. Q.; Zhang, X. Y.; Chen, Z. Y.; Gao, Y.; Yu, M.; Chen, D.; Pan, H. Z.; Liu, S. L.; Wang, D. S.; Mu, S. C. Constructing symmetry-mismatched $Ru_xFe_{3-x}O_4$ heterointerface-supported Ru clusters for efficient hydrogen evolution and oxidation reactions. *Nano Lett.* **2024**, *24*, 1015–1023.

[45] Mu, X. Q.; Yuan, Y. T.; Hu, Y. J.; Zeng, W. H.; Peng, W.; Zhang, Y. F.; Liu, X. Y.; Liu, S. L.; Mu, S. C. Robust water/seawater-electrolysis hydrogen production at industrial-scale current densities by modulating built-in-outer electric field of catalytic substance. *Nano Energy* **2024**, *131*, 110216.